Int. J. Solids Structures Vol. 30, No. 9, pp. 1213–1238, 1993
Printed in Great Britain

0020–7683/93 $6.00+ .00
Pergamon Press Ltd

EFFECTS OF FIBER AND INTERFACIAL LAYER MORPHOLOGIES ON THE THERMOPLASTIC RESPONSE OF METAL MATRIX COMPOSITES

MAREK-JERZY PINDERA
Civil Engineering and Applied Mechanics Department, University of Virginia, Charlottesville, VA 22903, U.S.A.

ALAN D. FREED and STEVEN M. ARNOLD
NASA-Lewis Research Center, Cleveland, OH 44135, U.S.A.

(*Received* 10 *March* 1992; *in revised form* 12 *October* 1992)

Abstract—This paper examines the effect of fiber and interfacial layer morphologies on thermal stress fields in metal matrix composites (MMCs). A micromechanics model based on an arbitrarily layered concentric cylinder configuration is used to calculate thermal stress fields in MMCs subjected to spatially uniform temperature changes. The fiber is modeled as a layered material with isotropic or orthotropic, elastic layers whereas the surrounding matrix, including interfacial layers, is treated as a strain-hardening, elasto–plastic, von Mises solid with temperature-dependent parameters. The solution to the boundary-value problem of an arbitrarily layered concentric cylinder under the prescribed thermal loading is obtained using the local/global stiffness matrix formulation originally developed for stress analysis of multilayered elastic media. Examples are provided that illustrate how the morphology of the SCS6 silicon carbide fiber and the use of multiple compliant layers at the fiber–matrix interface affect the evolution of residual stresses in SiC–Ti composites during fabrication cool-down.

INTRODUCTION

Modeling the thermal response of metal matrix composites continues to be an active and important area of research in composite mechanics. This is motivated, largely, by current efforts to develop a new generation of propulsion engines and structural components for use in a high-speed civil transport for the next century. Metal matrix composites are viable candidates for such applications because of their potentially superior properties at elevated temperatures. Large temperature changes however, either due to processing or actual in-service exposure, lead to high internal thermal stresses caused by a large mismatch in the thermal expansion coefficients of the fiber and matrix phases. These thermal stresses can be sufficiently large to yield the matrix during the fabrication process and/or subsequent service, altering the initial yield surfaces and subsequent hardening response (Aboudi, 1985; Fujita *et al.*, 1990). Radial cracking of the matrix at the fiber–matrix interface caused by circumferential stresses induced during fabrication cool-down has also been observed in certain types of material systems such as silicon carbide–titanium aluminide composites (SiC/Ti-Al) (Brindley *et al.*, 1990).

In addition to radial cracking, longitudinal and circumferential cracks at the fiber–matrix interface are also a source of concern (Johnson *et al.*, 1990; Brindley *et al.*, 1992). The longitudinal cracks can be particularly detrimental as they may result in fiber fractures, directly affecting the composite's strength. The interfacial cracks or debonds, observed in MMCs such as SiC–Ti in the presence of relatively low transverse stresses, can enhance matrix plasticity, leading to large plastic strains under biaxial loading and thus potential loss of structural stability (Lissenden *et al.*, 1992a,b).

A number of micromechanical approaches have been employed to model the thermal response of metal matrix composites in order to understand the influence of the constituent properties on the evolution of thermal stresses and on the overall effective response. These range from simple models utilizing combinations of the Reuss and Voigt hypotheses for the state of stress and strain in the fiber and matrix phases, and composite cylinder models, to periodic fiber array models based on approximate or rigorous geometrical and analytical

assumptions (Dvorak, 1990; Aboudi, 1991). In the majority of these approaches, the fiber is treated as homogeneous, elastic and isotropic or transversely isotropic.

Most recently, microstructures of different types of fibers used in advanced composites have been taken into account in modeling the thermal response. Avery and Herakovich (1986), for instance, have investigated the evolution of residual stresses in polymeric matrix composites with radially and circumferentially orthotropic, homogeneous, graphite fibers using the composite cylinder assemblage model. Warwick and Clyne (1991) modeled the SiC fiber as a two- and three-layered microstructure with isotropic and transversely isotropic sublayers in determining the residual stresses in SiC–Ti composites using a similar methodology to that employed by Avery and Herakovich. In the above references, the matrix was treated as elastic with temperature-independent properties.

The work by DiCarlo (1988), Wawner (1988), Lerch *et al.* (1988), and others indicates that certain types of silicon carbide fibers used in SiC–Ti composites, such as the SCS6 fiber, consist of at least five concentric isotropic and orthotropic layers, as illustrated in Fig. 1. The core of the fiber is carbon surrounded by a thin layer of pyrolytic graphite. This is followed by layers of short-grained and long-grained SiC material encased in an external carbon-rich coating. [We note that a recent microstructural investigation of the SCS6 fiber conducted by Ning and Pirouz (1991) indicates the presence of four distinct SiC regions.] The external carbon coating itself is composed of sublayers with different proportions of atomic elements. In order to be able to model such fiber microstructures, Sutcu (1992) developed a recursive concentric cylinder model for the thermomechanical response of composites, and used it to determine the thermal stresses in a SCS6 SiC/Ti-Al system. The analysis was conducted assuming elastic, temperature-independent properties of the phases.

Still another microstructural detail that most recently has been incorporated into various micromechanical models is the interfacial layer between the fiber and matrix phases. Such a layer can arise naturally due to a chemical reaction at the fiber–matrix interface, or is deliberately introduced to reduce residual stresses induced during the fabrication cool-down. In the latter instance, the idea is to tailor the geometry, thermal and elastoplastic properties of the interfacial layer in a way that reduces or "smooths out" the apparent thermal expansion mismatch between the fiber and matrix phases. The utility of this concept has been investigated by Arnold and co-workers (1990, 1992). Using the composite cylinder micromechanics model and the finite-element approach, these authors studied the evolution of residual thermal stresses in SiC–Ti_3Al systems for different combinations of thermo-elastoplastic properties of an interfacial layer. The feasibility of using a compliant or compensating layer in reducing residual stresses at the fiber–matrix interface was demonstrated, and the important parameters that govern the evolution of residual stresses in the presence of such a layer were identified.

In this paper, an analytical solution to a micromechanics model for the thermoplastic response of metal matrix composites is presented that is capable of efficiently accommodating various morphologies of layered fibers, such as silicon carbide, and different architectures of interfacial layers within a unified framework. The solution is constructed in a general manner that allows consideration of *arbitrary* fiber or interfacial layer configurations without the need to resolve the problem for a particular material system. In addition, the solution is extremely well suited for computer implementation. The presented analytical solution thus facilitates not only efficient parametric studies necessary in the course of developing new composite materials, but also design of engineered interfaces for improved performance. Further, the presented solution can readily be incorporated into an optimization algorithm in order to efficiently identify optimal configurations or morphologies for given applications.

The micromechanics model is based on the concentric cylinder assemblage, consisting of an arbitrary number of elastic or elastoplastic sublayers with isotropic or orthotropic, temperature-dependent properties, that is subjected to axisymmetric thermal loading. For this type of loading, the model yields realistic distributions of stress and displacement fields in the individual phases of a unidirectional composite away from the free edges, and thus can be employed to identify potential failure modes that may become activated by the residual stresses induced during fabrication cool-down. However, since the model is based

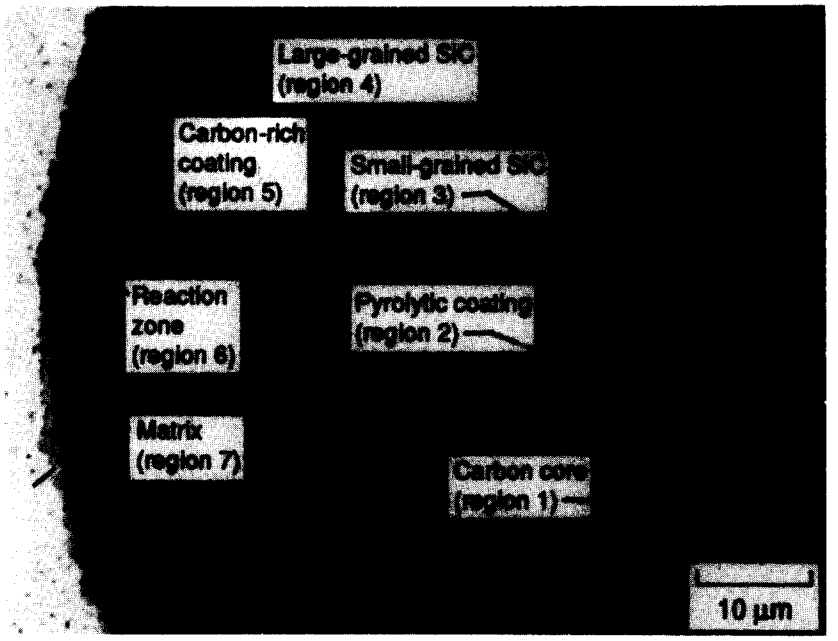

Fig. 1. Microstructure of a SiC fiber [courtesy of Lerch *et al.* (1988)].

on axisymmetric stress fields, it cannot be used to predict interfacial failure near the free edge of a composite caused by the axial shear stress. An analytical solution to the thermal boundary-value problem of the concentric cylinder assemblage is obtained using the *local/global stiffness matrix formulation* originally developed by Bufler (1971) for analysing the response of multilayered, isotropic, elastic media. The application of this technique to problems dealing with the elastic response of composite materials and structures has been outlined by Pindera (1991). Derstine and Pindera (1989) used the method to solve the problem of an arbitrarily laminated graphite/epoxy tube under axisymmetric loading using the endochronic theory for the nonlinear response of the individual plies. Most recently, Pindera and Freed (1992a) showed how this technique can be applied to axisymmetric, elastoplastic, boundary-value problems in composite mechanics. The local/global stiffness matrix formulation allows one to easily incorporate any number of concentric shells with arbitrary elastoplastic properties into the concentric cylinder model, while reducing the number of equations required to ensure continuity of interfacial tractions and displacements between the adjacent layers.

The presented model is subsequently employed to illustrate the effects of the morphology of layered SiC fibers and multiple compliant layers at the fiber–matrix interface on the evolution of thermal stresses in SiC–Ti_3Al composites during fabrication cool-down. The use of multiple interfacial layers has been suggested by Arnold *et al.* (1990) as a way of smoothing out the material property mismatch between the fiber and the surrounding matrix phase in order to optimize thermal stresses at the fiber–matrix interface. The present formulation facilitates modeling of the interfacial region as a region with spatially variable properties in order to investigate the effect of property gradients on thermal stress fields.

ANALYTICAL MODEL

We consider a long, cylindrical assemblage consisting of an arbitrary number of concentric cylinders or shells perfectly bonded to each other (Fig. 2). Each of the cylindrical shells may be either elastic or inelastic. The elastic shells may be isotropic, transversely isotropic, and radially or circumferentially orthotropic. The inelastic shells are taken as

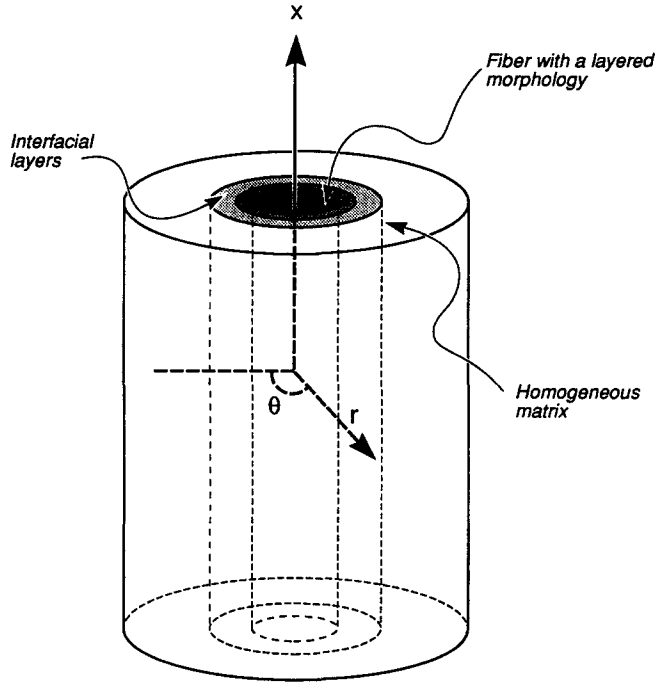

Fig. 2. Concentric cylinder model.

initially isotropic. It is assumed that all the material parameters governing the response of the elastic and inelastic layers may be functions of temperature. Although the analytical formulation is sufficiently general to admit time-dependent response of the individual layers, only time-independent plasticity will be considered here.

A distribution of displacements and stresses in the individual phases of the concentric composite cylinder model is sought under the conditions of a spatially uniform temperature change that varies with time. A solution of the outlined elastoplastic boundary-value problem is obtained using the displacement formulation. In what follows, the total strain formulation of the governing differential equations is employed within the framework of the so-called method of successive elastic solutions outlined by Mendelson (1983) for elastoplastic boundary-value problems.

In solving the outlined boundary-value problem, the following notation is adopted. The inner solid core is denoted by a subscript or superscript 1 and the outermost cylindrical shell by n. The inner radius of the kth shell is denoted by r_{k-1} and the outer radius by r_k. The traction and displacement components at the inner and outer radii of the kth shell are assigned superscripts "$-$" and "$+$", respectively.

For the prescribed axisymmetric loading, the longitudinal, tangential and radial displacement components u, v and w, referred to the cylindrical coordinate system x–r–θ centered at the origin of the concentric cylinder assemblage have the form:

$$u = u(x) = \varepsilon_0 x, \quad v = 0, \quad w = w(r), \tag{1}$$

where ε_0 is the same uniform longitudinal strain for all layers. These displacement components yield the following strain components in the cylindrical coordinate system:

$$\varepsilon_{xx} = \frac{\mathrm{d}u}{\mathrm{d}x} = \varepsilon_0, \quad \varepsilon_{\theta\theta} = \frac{w(r)}{r}, \quad \varepsilon_{rr} = \frac{\mathrm{d}w(r)}{\mathrm{d}r}, \tag{2}$$

with the shear strain components identically zero. Since the strain components are either constant or functions of only the radial coordinate r, the stress components are, at most, functions of r, and so the stress equilibrium equations in cylindrical coordinates reduce to the single equation:

$$\frac{\mathrm{d}\sigma_{rr}}{\mathrm{d}r} + \frac{\sigma_{rr} - \sigma_{\theta\theta}}{r} = 0. \tag{3}$$

The governing differential equation for the radial displacement $w(r)$ in each shell is obtained by expressing the stress components σ_{rr} and $\sigma_{\theta\theta}$ in eqn (3) in terms of $w(r)$ and its gradient using stress–strain equations and strain–displacement relations given by eqn (2). For problems in cylindrical coordinates, the stress–strain equations for an orthotropic material in the presence of thermal loading and inelastic effects, and in the absence of shear strains, are given by:

$$\begin{Bmatrix} \sigma_{xx} \\ \sigma_{\theta\theta} \\ \sigma_{rr} \end{Bmatrix} = \begin{bmatrix} C_{xx} C_{x\theta} C_{xr} \\ C_{x\theta} C_{\theta\theta} C_{\theta r} \\ C_{xr} C_{\theta r} C_{rr} \end{bmatrix} \begin{Bmatrix} \varepsilon_{xx} - \varepsilon_{xx}^{\mathrm{in}} - \alpha_{xx}(T - T_0) \\ \varepsilon_{\theta\theta} - \varepsilon_{\theta\theta}^{\mathrm{in}} - \alpha_{\theta\theta}(T - T_0) \\ \varepsilon_{rr} - \varepsilon_{rr}^{\mathrm{in}} - \alpha_{rr}(T - T_0) \end{Bmatrix}. \tag{4}$$

In the above, ε_{xx}, $\varepsilon_{\theta\theta}$, ε_{rr} are total strains, $\varepsilon_{xx}^{\mathrm{in}}$, $\varepsilon_{\theta\theta}^{\mathrm{in}}$, $\varepsilon_{rr}^{\mathrm{in}}$ are inelastic strains, and $\alpha_{xx}(T - T_0)$, $\alpha_{\theta\theta}(T - T_0)$, $\alpha_{rr}(T - T_0)$ are thermal strains, with T_0 denoting a reference temperature and T denoting the current temperature.

By introducing eqn (4) into the stress equilibrium equation [eqn (3)], and taking advantage of eqn (2), the following differential equations for the distribution of the radial displacement in the kth shell are obtained.

Transversely isotropic, elastic layers ($C_{x\theta} = C_{xr}$, $C_{\theta\theta} = C_{rr}$, $\alpha_{\theta\theta} = \alpha_{rr}$)

$$\frac{d^2w}{dr^2} + \frac{1}{r}\frac{dw}{dr} - \frac{w}{r^2} = 0. \tag{5a}$$

Orthotropic, elastic layers

$$\frac{d^2w}{dr^2} + \frac{1}{r}\frac{dw}{dr} - \frac{1}{r^2}\frac{C_{\theta\theta}}{C_{rr}}w = \frac{1}{r}\left[\frac{(C_{\theta x} - C_{xr})}{C_{rr}}\varepsilon_0 + \sum_{i=x,\theta,r}\frac{(C_{ri} - C_{\theta i})}{C_{rr}}\alpha_{ii}(T - T_0)\right]. \tag{5b}$$

Isotropic, inelastic layers

$$\frac{d^2w}{dr^2} + \frac{1}{r}\frac{dw}{dr} - \frac{1}{r^2}w = \frac{1}{r}\sum_{i=x,\theta,r}\frac{(C_{ri} - C_{\theta i})}{C_{rr}}\varepsilon_{ii}^{in}(r) + \frac{d}{dr}\sum_{i=x,\theta,r}\frac{C_{ri}}{C_{rr}}\varepsilon_{ii}^{in}(r), \tag{5c}$$

where the distribution of the inelastic strains, $\varepsilon_{ii}^{in}(r)$, is assumed to be known at the beginning of each thermal load increment.

The solution to the above equations is obtained subject to the boundary condition

$$\sigma_{rr}(r_n) = 0, \tag{6}$$

the interfacial displacement and traction continuity conditions

$$w_{k-1}(r_{k-1}) = w_k(r_{k-1}), \quad \sigma_{rr}^{k-1}(r_{k-1}) = \sigma_{rr}^{k}(r_{k-1}), \tag{7}$$

and the longitudinal equilibrium condition

$$\int_{A_c} \sigma_{xx}\, dA_c = 0, \tag{8}$$

where A_c is the cross-sectional area of the concentric cylinder assemblage.

Using standard techniques, solutions to the governing differential equations are obtained in the following form.

Transversely, isotropic, elastic layers

$$w(r) = A_1 r + \frac{A_2}{r}. \tag{9a}$$

Orthotropic, elastic layers

$$w(r) = A_1 r^{\lambda} + A_2 r^{-\lambda} + \frac{(C_{\theta x} - C_{rx})}{(C_{rr} - C_{\theta\theta})} r\varepsilon_0 + \sum_{i=x,\theta,r}\frac{(C_{ri} - C_{\theta i})}{(C_{rr} - C_{\theta\theta})}\alpha_{ii} r(T - T_0), \tag{9b}$$

where $\lambda = (C_{\theta\theta}/C_{rr})^{1/2}$.

Isotropic, inelastic layers

$$w(r) = A_1 r + \frac{A_2}{r} + \frac{1}{2r}\int_{r_{k-1}}^{r} \sum_{i=x,\theta,r} \frac{(C_{ri}+C_{\theta i})}{C_{rr}} \varepsilon_{ii}^{in}(r') r' \, dr'$$
$$+ \frac{r}{2}\int_{r_{k-1}}^{r} \sum_{i=x,\theta,r} \frac{(C_{ri}-C_{\theta i})}{C_{rr}} \varepsilon_{ii}^{in}(r') \frac{dr'}{r'} + \frac{1}{2}\sum_{i=x,\theta,r} \frac{C_{ri}}{C_{rr}} \varepsilon_{ii}^{in}(r_{k-1}) r \left(\frac{r_{k-1}^2}{r^2} - 1\right), \quad (9c)$$

where $r_{k-1} \leqslant r \leqslant r_k$.

The above solutions contain unknown coefficients A_1^k and A_2^k for each layer, as well as the unknown, uniform axial strain ε_0. For the solid core, the constant A_2^1 vanishes since the radial displacement at the center has to vanish. These unknown coefficients are determined from the boundary condition, interfacial traction and displacement continuity conditions, and the longitudinal force equilibrium condition. Application of these conditions yields a system of equations in the unknown A_1^k and A_2^k coefficients and the uniform longitudinal strain ε_0, that is solved iteratively when the inelastic strains are present. An iterative procedure is required because the inelastic strains depend implicitly on the unknown coefficients A_1^k and A_2^k. One such iterative procedure has been proposed by Mendelson (1983) in the presence of plastic strains. This procedure will be employed in the present analysis.

In order to automate the construction of this system of equations so that any arbitrarily layered configuration can easily be considered, we reformulate the problem in terms of the interfacial radial displacements as the basic unknowns in place of the coefficients A_1^k and A_2^k by using the concept of a *local stiffness matrix*. The local stiffness matrix relates the interfacial tractions at the inner and outer radii of the kth layer to the corresponding interfacial radial displacements, and is obtained from the solutions to eqns (5a)–(5c) [i.e. eqns (9a)–(9c)] in conjunction with the constitutive equations and strain–displacement equations [eqns (4) and (2)]. To construct the local stiffness matrix for the kth layer, we first express the coefficients A_1^k and A_2^k in terms of the interfacial displacements $w_k(r_{k-1})$ and $w_k(r_k)$ by evaluating the solutions for the radial displacement component $w(r)$ at the appropriate locations. These expressions are then used in the equations for the radial stress component in the kth layer given in terms of the determined radial displacement field. The final step entails an evaluation of the radial stress in the kth layer at the inner and outer radii in order to generate the radial tractions at those locations.

The form of the local stiffness matrix equation for the kth layer in the state of generalized plane strain and in the presence of thermal and inelastic effects is

$$\begin{Bmatrix} -\sigma_{rr}^- \\ \sigma_{rr}^+ \end{Bmatrix}^k = \begin{bmatrix} k_{11} & k_{12} \\ k_{21} & k_{22} \end{bmatrix}^k \begin{Bmatrix} w^- \\ w^+ \end{Bmatrix}_k + \begin{Bmatrix} k_{13} \\ k_{23} \end{Bmatrix}^k \varepsilon_0 + \begin{Bmatrix} f_1 \\ f_2 \end{Bmatrix}^k (T - T_0) + \begin{Bmatrix} g_1 \\ g_2 \end{Bmatrix}^k. \quad (10)$$

The thermal effects are represented by f_1^k and f_2^k, which are functions of the thermal expansion coefficients for the kth layer. The plastic effects are represented by g_1^k and g_2^k, which are given in terms of the integrals of the plastic strain distribution in the given layer. The elements $k_{11}^k, \ldots, k_{23}^k$ of the local stiffness matrix are functions of the geometry and elastic material properties of the kth layer (which may vary with temperature). These elements are given in the Appendix for transversely isotropic and orthotropic, elastic layers, and isotropic, inelastic layers. We note that the inelastic effects do not appear in the elements k_{ij}. This has certain advantages that will be pointed out later.

For the solid core, the coefficient A_2^1 in eqns (9a)–(9c) vanishes because the radial displacement w_1^- has to vanish, and so the relationship between the radial traction $\sigma_{rr}^1(r_1)$ at the outer radius of the core and the corresponding radial displacement simplifies to:

$$\sigma_{rr}^{1+} = k_{22}^1 w_1^+ + k_{23}^1 \varepsilon_0 + f_2^1 (T - T_0) + g_2^1. \quad (11)$$

Imposition of continuity of displacements and tractions along the common interfaces

[eqn (7)], together with the boundary condition on the radial stress at r_n [eqn (6)], and the longitudinal equilibrium condition specified by eqn (8), gives rise to a system of equations in the unknown interfacial displacements. The continuity of interfacial stresses is guaranteed by requiring that the sum of the tractions acting at the kth interface be zero, i.e.

$$\sigma_{rr}^{k+} + -\sigma_{rr}^{(k+1)+} = 0, \quad k = 1, \ldots, n-1, \tag{12}$$

whereas the continuity of interfacial displacements is directly enforced by requiring the common interfacial displacement w_k in the expressions for tractions given by eqn (10) to be

$$w_k = w_k^+ = w_{k+1}^-. \tag{13}$$

The system of equations is constructed by applying eqn (12) to each interface, starting with the inner interface between the core and the first cylindrical shell, in conjunction with the common interfacial displacements defined by eqn (13). This procedure yields the following equations:

$$\begin{aligned}
(k_{22}^1+k_{11}^2)w_1+k_{12}^2w_2+(k_{23}^1+k_{13}^2)\varepsilon_0 &= -(f_2^1+f_1^2)(T-T_0)-(g_2^1+g_1^2),\\
k_{21}^k w_{k-1}+(k_{22}^k+k_{11}^{k+1})w_k+k_{12}^{k+1}w_{k+1}+(k_{23}^k+k_{13}^{k+1})\varepsilon_0 &\\
= -(f_2^k+f_1^{k+1})(T-T_0)-(g_2^k+g_1^{k+1}),&\\
k_{21}^n w_{n-1}+k_{22}^n w_n+k_{23}^n\varepsilon_0 = -f_2^n(T-T_0)-g_2^n,&
\end{aligned} \tag{14}$$

where n is the number of cylindrical shells including the core. The remaining equation necessary for the solution of the system of equations for the unknown interfacial displacements w_k and the axial strain ε_0 is provided by the longitudinal equilibrium condition [eqn (8)]. This yields:

$$\begin{aligned}
(\phi_{22}^1+\phi_{11}^2)w_1\cdots+\cdots(\phi_{22}^k+\phi_{11}^{k+1})w_k\cdots+\cdots\phi_{22}^n w_n+\sum_{k=1}^{n}\psi_k\varepsilon_0 &\\
= -\sum_{k=1}^{n}\Omega_k(T-T_0)-\sum_{k=1}^{n}\Pi_k,&
\end{aligned} \tag{15}$$

where ϕ_{11}^k, ϕ_{22}^k, ψ_k, Ω_k and Π_k are also given in the Appendix.

The system of equations comprised of eqns (14) and (15) can be represented in the matrix form shown below. We observe that the global stiffness matrix is constructed by first superposing the local stiffness matrices along the main diagonal in an overlapping fashion, and then adding a column and a row to account for the thermal effects and the longitudinal equilibrium condition in the case of free thermal expansion/contraction. Under the conditions of plane strain, ε_0 vanishes and the $(n+1)$th row and column are not added into the global stiffness matrix. It is a simple matter to construct a computer algorithm for assembling the global stiffness matrix:

$$\begin{bmatrix}
k_{22}^1+k_{11}^2 & k_{12}^2 & 0 & \cdot & k_{23}^1+k_{13}^2\\
k_{21}^2 & k_{22}^2+k_{11}^3 & \cdot & \cdot & \cdot\\
0 & k_{21}^3 & \cdot & \cdot & \cdot\\
\cdot & \cdot & \cdot & k_{22}^n & k_{23}^n\\
\phi_{22}^1+\phi_{11}^2 & \cdot & \cdot & \phi_{22}^n & \sum\psi_k
\end{bmatrix}
\begin{Bmatrix} w_1\\ w_2\\ \cdot\\ w_n\\ \varepsilon_0 \end{Bmatrix}$$

$$= -\begin{Bmatrix} f_2^1+f_1^2\\ \cdot\\ \cdot\\ f_2^n\\ \sum\Omega_k \end{Bmatrix}(T-T_0)-\begin{Bmatrix} g_2^1+g_1^2\\ \cdot\\ \cdot\\ g_2^n\\ \sum\Pi_k \end{Bmatrix}. \tag{16}$$

The outlined reformulation of the elastoplastic boundary-value problem for an arbitrary concentric cylinder assemblage using the local/global stiffness matrix approach has the following advantages: automatic satisfaction of interfacial continuity conditions in a pointwise fashion; reduction in the number of the boundary condition and continuity equations by nearly 50% for large numbers of concentric cylinders; and automatic assembly of the global stiffness matrix, facilitating the addition of concentric cylinders without additional effort. Furthermore, as the elements of the stiffness matrices for different types of layers have been provided in closed form, the outlined thermal boundary-value problem does not have to be resolved each time a particular concentric cylinder assemblage is considered. Different configurations are efficiently handled by assembling the global stiffness matrix in an appropriate fashion using the provided local stiffness matrices.

SOLUTION PROCEDURE

The system of equations given by eqn (16) is solved iteratively at each temperature step for the specified loading after the manner suggested by Mendelson (1983). The iteration is performed on the plastic force vector that consists of the elements g_1^k, g_2^k and $\Sigma \Pi_k$. These are expressed in terms of the integrals of the plastic strain distributions in the given layer that have the form (see the Appendix):

$$\int_{r_{k-1}}^{r_k} \sum_{i=x,\theta,r} \frac{(C_{ri}+C_{\theta i})}{C_{rr}} \varepsilon_{ii}^{in}(r') r' \, dr', \quad \int_{r_{k-1}}^{r_k} \sum_{i=x,\theta,r} \frac{(C_{ri}-C_{\theta i})}{C_{rr}} \varepsilon_{ii}^{in}(r') \frac{dr'}{r'}. \tag{17}$$

Since the elements of the global stiffness matrix at a given temperature are constant, only one inversion of the matrix for each sequence of iterations is required. As the elements f_1^k, f_2^k and $\Sigma \Omega_k$ of the thermal force vector are constant at a given temperature, most of the computational effort lies in evaluating the integrals in eqn (17) at each iteration. The algorithm for the iterative procedure is given in the sequel.

For the given temperature increment, the plastic strain distribution in each layer is expressed in terms of the distribution at the preceding temperature plus an increment that results from the imposed temperature change:

$$\varepsilon_{ij}^p(r)|_{\text{current}} = \varepsilon_{ij}^p(r)|_{\text{previous}} + d\varepsilon_{ij}^p(r). \tag{18}$$

The plastic strain increment is derived from the von Mises yield condition which, in the presence of temperature-dependent elastoplastic properties of the matrix phase, has the form

$$F = \tfrac{1}{2}\sigma'_{ij}\sigma'_{ij} - \tfrac{1}{3}\bar{\sigma}^2(\bar{\varepsilon}^p, T) = 0, \tag{19}$$

where $\bar{\sigma}$ is the effective yield stress, which is a function of both the effective plastic strain $\bar{\varepsilon}^p$ and temperature. The plastic strain increment is thus,

$$d\varepsilon_{ij}^p = \frac{\partial F}{\partial \sigma'_{ij}} d\lambda = \sigma'_{ij} \, d\lambda, \tag{20}$$

where the proportionality constant $d\lambda$ is obtained from the consistency condition for plastic loading in the form

$$d\lambda = \frac{\sigma'_{ij} D_{ijkl}(d\varepsilon_{kl} - d\varepsilon^{th}_{kl}) + \left(\sigma'_{ij} C'_{ij} - \frac{2}{3}\bar{\sigma}\frac{\partial \bar{\sigma}}{\partial T}\right) dT}{\frac{4}{9}\bar{\sigma}^2 \frac{\partial \bar{\sigma}}{\partial \bar{\varepsilon}^p} + \sigma'_{ij} D_{ijkl} \sigma'_{kl}}, \tag{21}$$

where $d\lambda \geqslant 0$ for plastic loading, $d\lambda \leqslant 0$ for neutral loading or unloading, and $d\varepsilon^{th}_{ij}$ are the thermal strain increments given by

$$d\varepsilon^{th}_{ij} = \left[\alpha_{ij}(T) + \frac{\partial \alpha_{ij}(T)}{\partial T}(T - T_0)\right] dT, \tag{22}$$

where D_{ijkl} are the elastic stiffness elements, and $C'_{ij} = (\partial D_{ijkl}/\partial T)\varepsilon^e_{kl}$. In the present investigation, the elastoplastic stress–strain response of the matrix is taken to be bilinear so that the slope of the effective stress–plastic strain curve, $\partial \bar{\sigma}/\partial \bar{\varepsilon}_p$, is constant at a given temperature. Since the incremental theory of plasticity is used to calculate the plastic strain increment at each point along the radial coordinate, the inelastic analysis is valid for both loading and unloading in the plastic phases.

The plastic strain distribution in each layer is determined by calculating the plastic strains at 21 stations after updating the plastic strains at these locations using eqn (18). The current values for the plastic strains at these stations are then used in determining the integrals given in eqn (17), and thus the elements of the plastic force vector in eqn (16). Updated values of the interfacial displacements are then obtained using eqn (16). With a knowledge of the interfacial displacements and the axial strain ε_0, the coefficients A^k_1 and A^k_2 in each layer can be obtained, producing solutions for the radial displacement $w_k(r)$ from which radial and tangential total and plastic strains, and the corresponding stresses, can be obtained. These are then used to obtain new approximations for the plastic strain increments. The iterative process is terminated when the differences between two successive sets of plastic strain increments are less than some prescribed value. The above procedure is described in detail by Mendelson (1983).

APPLICATIONS

As an application of the outlined method, we investigate residual stresses in a concentric cylinder consisting of a SCS6 SiC fiber surrounded by a layer of titanium matrix that is subjected to a temperature change of $-792°C$ (Arnold *et al.*, 1990). Two cases are considered, namely, a layered fiber embedded in a homogeneous matrix, and a homogeneous fiber embedded in a matrix with a layered interface. In both cases, the outer radius of the composite cylinder was normalized to 1.0, with the normalized fiber radius of 0.6320 producing a fiber volume fraction of 0.40. For the second case, the interfacial layer outer radius was 0.6952, resulting in an interfacial volume fraction of 0.08.

The calculations were performed using temperature increments of $\Delta T = -1.39°C$. Convergence of plastic strain increments at the various radial locations typically did not require more than 10 iterations at each temperature increment. As an additional check, values of the effective stress calculated from the effective stress–plastic strain curve at various radial locations were compared with values of the effective stress based on the obtained stress components at these locations. Typically, differences were a fraction of a percent. As a final check of the accuracy of the analytical solution, axial, circumferential and radial stress profiles generated during the fabrication cool-down of a homogeneous SiC fiber with a single interfacial layer embedded in a titanium matrix were compared with the corresponding results obtained with the commercially available finite-element program ABAQUS (1989). The material properties of the fiber and matrix phases used in the

Table 1. Material properties of homogeneous SiC fiber and titanium matrix (Arnold *et al.*, 1990)

Material properties	24°C	200°C	425°C	600°C	650°C	815°C
Homogeneous SiC fiber						
$\alpha(\times 10^{-6}$ cm cm^{-1} °C$^{-1})$	3.53	3.62	3.87	4.19	4.28	4.5
Young's modulus (GPa)	400.0	400.0	400.0	400.0	400.0	400.0
Poisson's ratio	0.25	0.25	0.25	0.25	0.25	0.25
Ti-24Al-11Nb matrix						
$\alpha(\times 10^{-6}$ cm cm^{-1} °C$^{-1})$	9.0	9.36	10.26	10.53	10.62	11.07
Young's modulus (GPa)	110.3	100.0	75.8	86.2	68.2	11.2
Poisson's ratio	0.26	0.26	0.26	0.26	0.26	0.26
Yield stress (MPa)	371.5	406.7	370.2	290.9	269.5	165.5
Hardening slope (GPa)	22.98	3.04	2.22	1.29	0.67	0.00

calculations are given in Table 1. The elastoplastic and thermal properties of the interfacial layer (with the exception of the Poisson's ratio) were taken to be one half and two times those of the matrix properties respectively, at each temperature. A quarter-symmetry mesh was constructed that consisted of triangular (CGPE8) and quadrilateral (CGPE10), generalized plane strain elements. A total of 580 elements was employed. The applied boundary conditions modeled the axisymmetric thermal loading. Selected comparison of the three stress components and the radial displacement at several radial locations in the fiber, interfacial layer and matrix obtained with the present analytical solution and the finite-element solution is presented in Table 2. Clearly, the differences are quite negligible. A more detailed comparison will be presented elsewhere.

Case I: Effect of fiber microstructure on thermal stresses

As mentioned previously, SCS6 SiC fibers exhibit composite microstructures consisting of a core surrounded by a number of cylindrical shells, with each region possessing generally different properties. In this work, the SCS6 SiC fiber is modeled using five regions with distinct properties. The inner carbon core (Region I in Fig. 1) is assumed to be isotropic, the pyrolytic layer (Region II) circumferentially orthotropic, the silicon carbide regions (Regions III and IV) radially orthotropic, and the outer carbon-rich coating (Region V) isotropic or circumferentially orthotropic. The evolution of residual stresses is investigated for a total of nine cases in view of the uncertainty associated with accurate determination of the material properties in the individual layers. For the first six cases, a common set of material properties is used in Regions I–IV, while one set of properties is used in the outer carbon-rich coating or Region V for cases 1–3 and another set for cases 4–6. In cases 1–3 the outer carbon-rich coating is taken to be isotropic, whereas in cases 4–6 it is assumed to

Table 2. Comparison of stresses at selected radial locations generated by the present model and ABAQUS

Radial location	σ_{xx} (MPa)	$\sigma_{\theta\theta}$ (MPa)	σ_{rr} (MPa)	$w(r)$ ($\times 10^{-4}$ m m^{-1})
0.6320 (fiber)				
Present model	−546.00	−128.50	−128.50	−0.4323
ABAQUS	−546.01	−128.49	−128.49	−0.4322
0.6320 (interfacial layer)				
Present model	245.15	266.73	−128.50	−0.4323
ABAQUS	245.51	266.85	−128.26	−0.4322
0.6952 (interfacial layer)				
Present model	264.87	251.01	−93.34	−0.9329
ABAQUS	265.32	251.21	−92.94	−0.9328
0.6952 (matrix)				
Present model	334.91	243.98	−93.34	−0.9329
ABAQUS	335.50	243.60	−93.14	−0.9328
1.0 (matrix)				
Present model	391.72	179.80	0.00	−1.6304
ABAQUS	391.70	179.79	0.07	−1.6303

be circumferentially orthotropic with the same properties as Region II. The remaining three cases (cases 7–9) are based on material properties of a SCS6 SiC fiber used in an earlier investigation (Pindera and Freed, 1992b) which are thought to be not as accurate as those employed for cases 1–6. Irrespective of the actual properties employed in the calculations, cases 1, 4 and 7 correspond to equal expansion coefficients of the two SiC layers in the axial, radial and circumferential directions, while for cases 2, 5 and 8, and cases 3, 6 and 9, the radial thermal expansion coefficient in the SiC layers is 25% greater and smaller, respectively, than the thermal expansion coefficients in the axial and circumferential directions.

The temperature-independent material parameters for the five different regions of the SiC fiber used in cases 1–6 are given in Table 3(a), whereas the corresponding temperature-dependent thermal expansion coefficients are given in Table 3(b). These properties are based on data compiled by Lara-Curzio and Sternstein (1992a,b) and DiCarlo (1992), and are thought to be the best properties for the individual regions of a SCS6 SiC fiber available at the present time. The temperature-dependent thermal expansion coefficients of the SiC regions (Regions III and IV) in Table 3(b) (cases 1 and 4) have been calculated using the empirical formula provided by Li and Bradt (1986) given in the form

$$\alpha_{SiC} = 3.19\times 10^{-6}+3.6\times 10^{-9}T-1.68\times 10^{-12}T^2(^{\circ}C^{-1}).$$

The properties of the different regions of a SCS6 SiC fiber used for cases 7–9 are given in Tables 4(a) and 4(b). As mentioned earlier, these properties are not as accurate as those provided in Tables (3a) and 3(b), and are used here for parametric and illustrative purposes. In particular, we point out that the two sets of properties given in Tables 3(a) and 3(b) and Tables 4(a) and 4(b), respectively, differ significantly in the pyrolytic and outer coatings (Regions II and V). They are identical in the SiC regions (Regions III and IV) and somewhat different in the carbon core (Region I).

The temperature-dependent material parameters of the titanium matrix used in the calculations are the same as those given in Table 1. Included in the table are the properties of the homogeneous SiC fiber employed by Arnold *et al.* (1990, 1992) in investigating the effectiveness of a compliant/compensating layer in reducing residual stresses in the matrix adjacent to the fiber-matrix interface. The results obtained, taking into account the SCS6

Table 3(a). Temperature-independent properties of different regions comprising a SCS6 SiC fiber, cases 1–6

Material properties	Region I†	Region II†	Region III†‡	Region IV†‡	Region V†
E_{xx} (GPa)	41.36	175.11	413.64	413.64	79.97/175.11
$E_{\theta\theta}$ (GPa)	41.36	175.11	413.64	413.64	79.97/175.11
E_{rr} (GPa)	41.36	6.89	482.58	579.10	79.97/6.89
ν_{xr}	0.24	1.875	0.19	0.19	0.30/1.875
$\nu_{x\theta}$	0.24	0.036	0.25	0.25	0.30/0.036
$\nu_{r\theta}$	0.24	0.075	0.19	0.19	0.30/0.075
α_{xx} ($\times 10^{-6}$ cm cm^{-1} °C^{-1})	9.99	1.80	see Table 3(b)	see Table 3(b)	8.80/1.80
$\alpha_{\theta\theta}$ ($\times 10^{-6}$ cm cm^{-1} °C^{-1})	9.99	1.80	see Table 3(b)	see Table 3(b)	8.80/1.80
α_{rr} ($\times 10^{-6}$ cm cm^{-1} °C^{-1})	9.99	27.99	see Table 3(b)	see Table 3(b)	8.80/27.99
Normalized outer radius	0.2232	0.2512	0.4698	0.9580	1.0000

† After Lara-Curzio and Sternstein (1992a, b).
‡ After DiCarlo (1992).

Table 3(b). Temperature-dependent thermal expansion coefficients of Regions III and IV of a SCS6 SiC fiber

α_{rr} ($\times 10^{-6}$ cm cm^{-1} °C^{-1})	24°C	200°C	425°C	600°C	650°C	815°C
Case 1 and 4: $\alpha_{rr}=\alpha_{xx}=\alpha_{\theta\theta}$†	3.28	3.83	4.50	4.99	5.11	5.45
Case 2 and 5: $\alpha_{rr}=1.25\alpha_{xx}=1.25\alpha_{\theta\theta}$	4.10	4.79	5.63	6.23	6.39	6.82
Case 3 and 6: $\alpha_{rr}=0.75\alpha_{xx}=0.75\alpha_{\theta\theta}$	2.47	2.88	3.38	3.74	3.83	4.09

† After Li and Bradt (1986).

Table 4(a). Temperature-independent properties of different regions of a SCS6 SiC fiber, cases 7–9

Material properties	Region I†	Region II†	Region III†	Region IV†	Region V†
E_{xx} (GPa)	27.58	220.61	413.64	413.64	27.58
$E_{\theta\theta}$ (GPa)	27.58	220.61	413.64	413.64	27.58
E_{rr} (GPa)	27.58	27.58	482.58	579.10	27.58
ν_{xr}	0.20	0.25	0.19	0.19	0.20
$\nu_{x\theta}$	0.20	0.20	0.25	0.25	0.20
$\nu_{r\theta}$	0.20	0.25	0.19	0.19	0.20
α_{xx} ($\times 10^{-6}$ cm cm^{-1} °C^{-1})	5.58	0.27	see Table 4(b)	see Table 4(b)	5.58
$\alpha_{\theta\theta}$ ($\times 10^{-6}$ cm cm^{-1} °C^{-1})	5.58	0.27	see Table 4(b)	see Table 4(b)	5.58
α_{rr} ($\times 10^{-6}$ cm cm^{-1} °C^{-1})	5.58	5.58	see Table 4(b)	see Table 4(b)	5.58
Normalized outer radius	0.2232	0.2512	0.4698	0.9580	1.0000

†After Pindera and Freed (1992b).

Table 4(b). Temperature-dependent thermal expansion coefficients of Regions III and IV of a SCS6 SiC fiber

α_{rr} ($\times 10^{-6}$ cm cm^{-1} °C^{-1})	24°C	200°C	425°C	600°C	650°C	815°C
Case 7: $\alpha_{rr} = \alpha_{xx} = \alpha_{\theta\theta}$†	3.53	3.62	3.87	4.19	4.28	4.50
Case 8: $\alpha_{rr} = 1.25\alpha_{xx} = 1.25\alpha_{\theta\theta}$	4.41	4.52	4.84	5.24	5.35	5.62
Case 9: $\alpha_{rr} = 0.75\alpha_{xx} = 0.75\alpha_{\theta\theta}$	2.65	2.72	2.90	3.15	3.22	3.38

†After Pindera and Freed (1992b).

SiC fiber's microstructure, are compared with the results generated assuming the fiber to be homogeneous.

The results for the axial, circumferential and radial stress distributions are presented in Figs 3(a)–(c), 4(a)–(c) and 5(a)–(c), respectively, for all the considered cases. The letter codes *a*, *b* and *c* in the above figures denote cases 1–3, 4–6, and 7–9, for each of the three stress profiles. The illustrated residual stress profiles indicate that the microstructure of the SiC fiber has a substantial influence on the stress distribution in the individual layers of the fiber, as suggested in the results obtained by previous investigators (Lekhnitskii, 1981; Avery and Herakovich, 1986). In particular, we note that in contrast with the uniform, negative, axial stress observed in the homogeneous fiber, the axial stress in the isotropic carbon core is positive for all the considered cases [Figs 3(a)–(c)]. The relatively high tensile stresses observed in the first six cases point to a potential failure of the carbon core for a sufficiently large tensile deformation applied to the composite in the fiber direction. In fact, given that the Young's modulus of the carbon core is 41.36 GPa [Table 3(a)], and neglecting stresses due to the Poisson's effect, an axial strain of 1% will generate an axial stress of 413.64 MPa in the core, that, together with the initial residual stress may be sufficient to fracture the core (McKee and Joo, 1972). For the last three cases, on the other hand, the axial stress in the carbon core is quite low. For cases 1–6 [Figs 3(a)–(b)], the pyrolytic coating is either in a state of axial compression or tension depending on the values of the thermal expansion coefficients in the SiC layers and the outer coating, while the axial stress distribution in the slightly radially orthotropic SiC layers depends on the thermal expansion coefficients in those layers. When the three coefficients are equal (cases 1 and 4), a nearly uniform distribution is observed. When the radial coefficient is greater than the remaining two (cases 2 and 5), the axial stress increases towards the core, whereas a decrease is observed when the radial coefficient is smaller (cases 3 and 6). The axial stress in the outer coating is positive for cases 1–3 and negative for cases 4–6. For cases 7–9 [Figure 3(c)], the pyrolytic coating is in a state of high axial compression regardless of the values of the thermal expansion coefficients in the SiC layers, while the axial stress distribution in the slightly radially orthotropic SiC layers follows the same trends observed in cases 1–6. The axial stress in the outer carbon coating is positive for cases 7–9 and small in magnitude in comparison with cases 1–6.

Similar trends are observed for the hoop stress distribution [Figs 4(a)–(c)]. In this case however, the distribution of the hoop stress within the SiC layers for cases 1–6 [Figs 4(a)–

(b)], is substantially more nonuniform in comparison with the corresponding axial stress cases [Figs 3(a)–(b)]. The large tensile values of the hoop stress in the outer carbon coating observed for cases 1–3 in Fig. 4(a) indicate a potential initiation site for radial microcracking. In fact, radial microcracks in the outer carbon-rich coating have been reported by Brindley *et al.* (1990) and MacKay *et al.* (1991). On the other hand, if the properties of the outer coating are the same as those of the pyrolytic layer with a large thermal expansion coefficient in the radial direction, a desirable compressive hoop stress develops in the outer coating as observed in Fig. 4(b) for cases 4–6, thereby removing the driver for radial cracking in this coating. For cases 7–9 [Fig. 4(c)], the variation of the hoop stress in the SiC layers with the thermal expansion coefficient is also much greater than in the corresponding axial stress case [Fig. 3(c)], while in the outer carbon coating the hoop stress is tensile and relatively small.

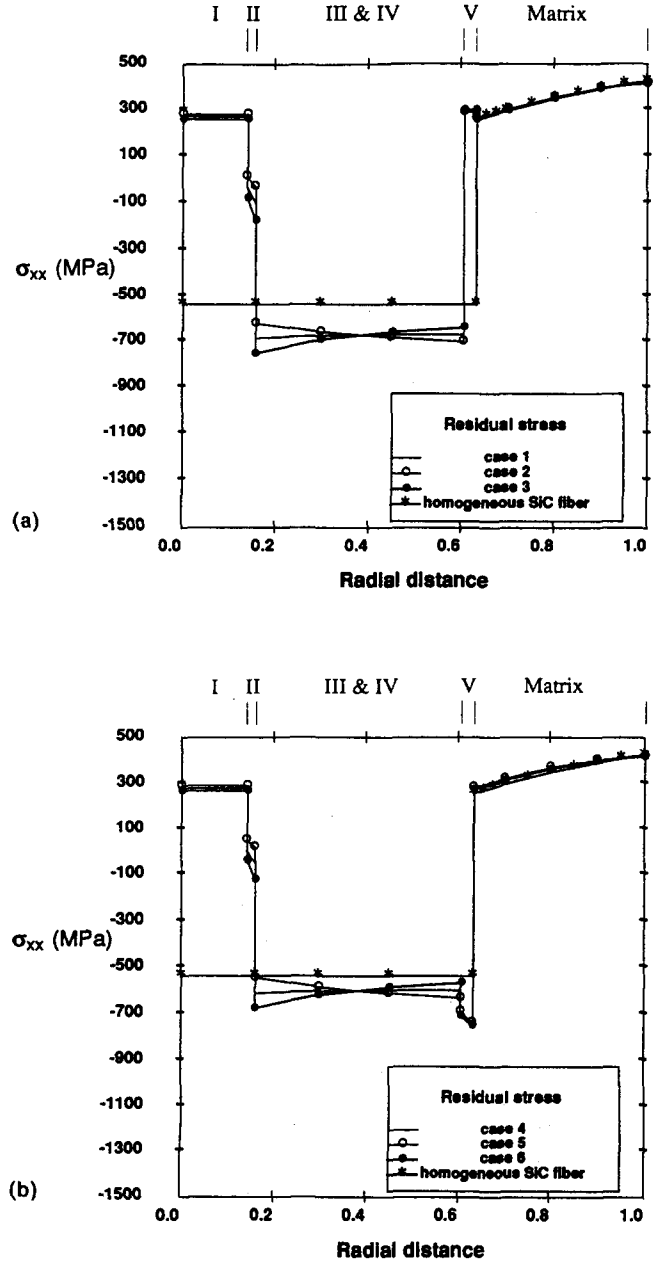

Fig. 3. The effect of fiber morphology on the axial stress in a concentric cylinder due to $\Delta T = -792°C$: (a) cases 1–3; (b) cases 4–6; (c) cases 7–9.

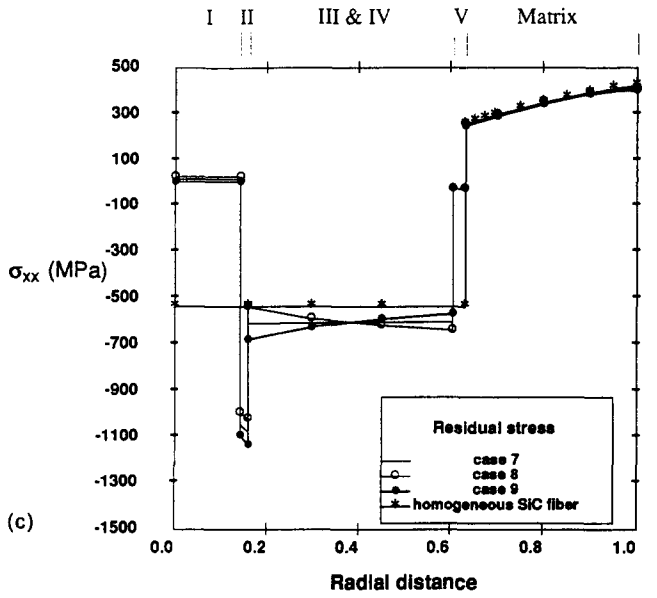

Fig. 3 (*continued*).

The radial stress distributions shown in Figs 5(a)–(b) for cases 1–6 indicate that the magnitude of the radial stress in the SiC layers directly adjacent to the outer carbon coating is affected by the thermal expansion coefficient of the outer coating. In particular, the stress profiles are shifted up, producing smaller magnitudes of compressive radial stress in the outer SiC layers when the outer coating has a high thermal expansion coefficient in the radial direction (cases 4–6). The form of the stress distribution, however, remains similar in both sets of cases, increasing monotonically with decreasing radial coordinate in the inner SiC region. Within each set of cases, the distribution of radial stresses in the SiC regions increases uniformly (i.e. shifts up) with increasing thermal expansion coefficient in that region. Relatively large differences are observed in the radial stress magnitudes in the SiC layers for the different values of the radial thermal expansion coefficient. In the vicinity of the carbon core, the largest radial stress is generated when the radial thermal expansion coefficient in the SiC regions is highest (cases 2 and 5). The relatively large tensile stresses observed at the interfaces separating the inner core from the pyrolytic coating, and the pyrolytic coating from the SiC regions, point to a potential debonding of these interfaces during either cool-down or upon tensile loading, given the poor radial properties of the circumferentially orthotropic pyrolytic coating and the large Poisson's ratio ν_{xr}. We note that if debonding were to take place between the carbon core and/or pyrolytic coating and the surrounding material during cool-down or subsequent tensile loading, the initially high residual axial stresses in the carbon core would relax, eliminating the possibility of failure in the core. In contrast with the first six cases, the radial stresses in the vicinity of the carbon core for cases 7–9 are either quite low or compressive as observed in Fig. 5(c). The general form of the radial stress distributions throughout the various fiber regions for these cases, however, is similar to the distributions observed in the preceding cases.

Perhaps the most important result gained from the data presented in Figs 3–5 is the observation that the microstructure of the SiC fiber has little effect on the elastoplastic stress distribution in the matrix phase for the range of the employed material parameters. From the point of view of radial cracking susceptibility at the fiber–matrix interface, the circumferential stress component $\sigma_{\theta\theta}$ plays the most important role. Figures 4(a)–(c) illustrate that the reduction in the circumferential stress depends on the thermal expansion coefficient of both the SiC regions and the outer carbon coating. Within each of the three sets of investigated cases, the biggest reduction in the circumferential stress in the matrix phase is obtained when the radial thermal expansion coefficient α_{rr} in the SiC regions is

25% greater than the longitudinal and circumferential thermal expansion coefficients, denoted by cases 2, 5 and 8 in the figures. This is clearly consistent with the physics of the deformation in the presence of constraining layers, and is further borne out by the corresponding reduction in the radial stress profile illustrated in Figs 5(a)–(c). The biggest reduction in the hoop stress for all the cases occurs for case 5 [Fig. 4(b)], when the radial thermal expansion coefficient of the outer carbon coating is very large in relation to that of the matrix. In this case, the outer coating acts as a compensating layer, as suggested by the results of Arnold *et al.* (1990, 1992), resulting in a further decrease of the matrix hoop stress. Clearly, however, the reductions in $\sigma_{\theta\theta}$ of the matrix are quite modest for all the considered cases. It appears that a substantially greater increase in either the radial thermal expansion coefficient of the SiC layers (for cases 2, 5 and 8), or the thickness of the

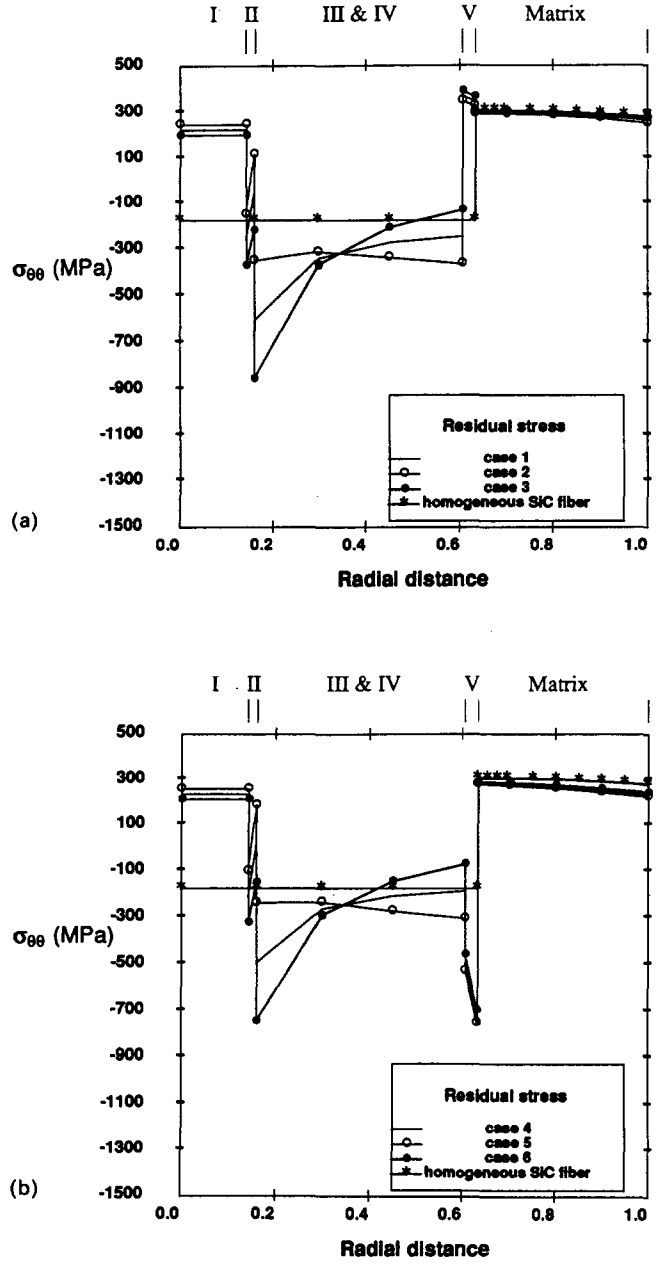

Fig. 4. The effect of fiber morphology on the hoop stress in a concentric cylinder due to $\Delta T = -792°C$: (a) cases 1–3; (b) cases 4–6; (c) cases 7–9.

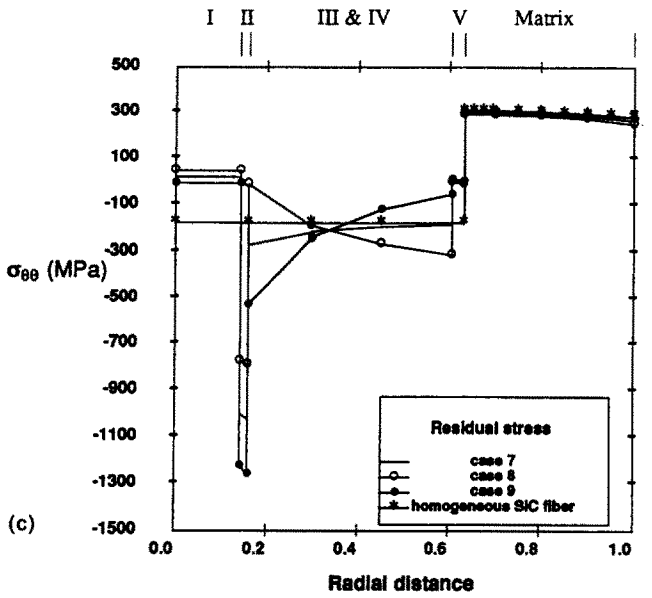

Fig. 4 (*continued*)

outer carbon coating (for cases 4–6), is required to produce a significant reduction of the circumferential stress in the matrix phase at the fiber–matrix interface.

Case II: Effect of interfacial layer morphology on thermal stresses

The work of Arnold *et al.* (1990, 1992) indicates that the most important interface layer parameters for reducing the matrix inplane stresses are the thermal expansion coefficient and the thickness of the layer. The thermal expansion coefficient should be chosen such that $\alpha^{layer} > \alpha^{matrix}$ and the thickness of the compliant layer should be as large as other considerations allow. For a given thickness of the interfacial layer, the matrix hoop stress decreases with increasing thermal expansion coefficient of the layer, suggesting that α^{layer} should be as large as possible in relation to α^{matrix}. However, the reduction in the matrix hoop stress is accompanied by an increase in the interfacial layer hoop stress itself. In fact, the interfacial layer hoop stress may exceed that in the matrix phase above a certain value of α^{layer}, potentially resulting in radial cracking in the interfacial layer itself. Elastic and inelastic properties of the interfacial layer appear to play a secondary role as far as the matrix inplane stresses are concerned. Since the results of Arnold *et al.* (1990, 1992) indicate that increasing the thermal expansion coefficient of the interfacial layer decreases the inplane stresses in the matrix at the expense of larger hoop stresses in the interfacial region, we ask whether grading the thermal expansion coefficient of the interfacial region using multiple layers offers any advantages over the use of a single interfacial layer with regard to optimizing hoop stresses in both the interfacial layer and the matrix phase. To answer this question, we consider the cases of two and three interfacial layers with different thermal expansion coefficients lying between two values, and compare the resulting stress distributions with those generated in the presence of a single interfacial layer with the two extremal thermal expansion coefficients.

The temperature-dependent material parameters of the fiber and matrix phases of the SiC–Ti_3Al composite used in the calculations are given in Table 1. The elastic and inelastic properties of the interfacial layers (excluding the Poisson's ratios) were taken to be one half of the corresponding matrix properties at each temperature. This choice is motivated by the observation of Arnold *et al.* (1990) that the elastic and inelastic properties of the interfacial layer should be as small as possible relative to those of the matrix as regards minimization of overall residual stress state. The thermal expansion coefficients of the interfacial layers were chosen in the following manner. First, stress distributions for single

interfacial layers having thermal expansion coefficients two and three times that of the matrix phase were generated independently. Those are indicated by open and solid circles in the figures that follow. Next, stress distributions in the presence of two interfacial layers were generated with each layer having thermal expansion coefficients two and three times that of the matrix phase. Finally, stress distributions were obtained in the presence of three layers, with the individual layers having thermal expansion coefficients of two, two and one half, and three times that of the matrix phase.

Figure 6 presents the hoop stress $\sigma_{\theta\theta}$ distributions in the fiber, interfacial layer(s) and the matrix phase for the cases of zero, one, two and three interfacial layers. In the cases of multiple interfacial layers, the thermal expansion coefficients were graded in a monotonically increasing manner from the inner to the outer interfacial layer. Inverting this grading

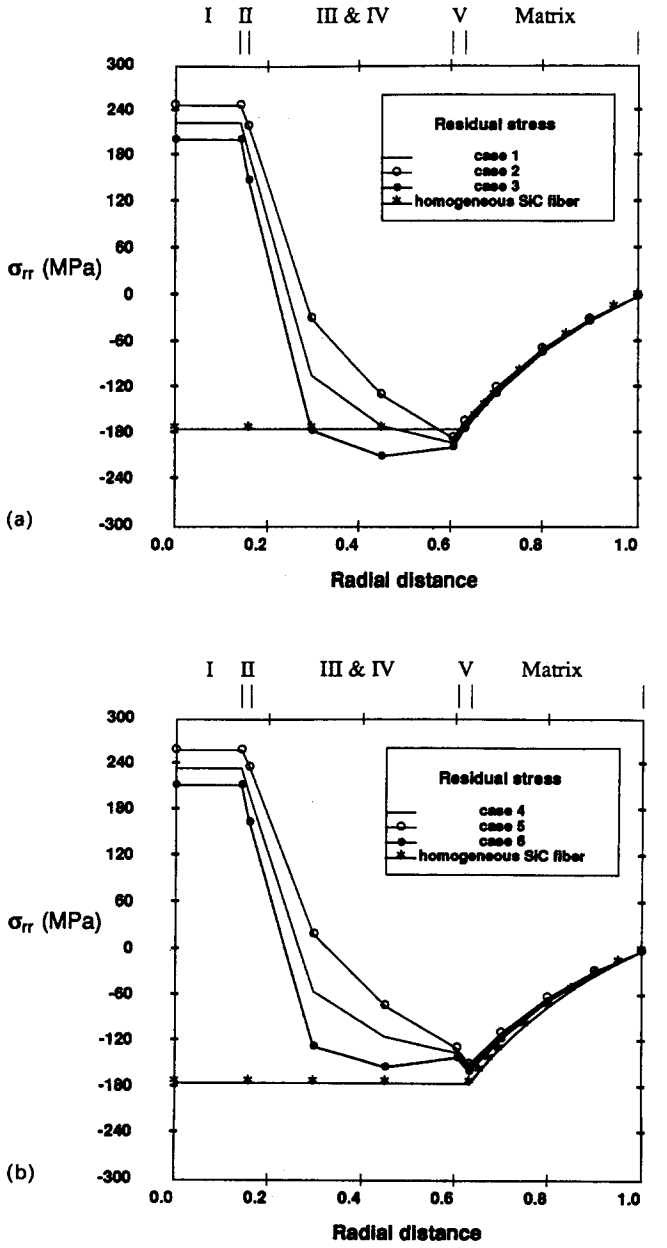

Fig. 5. The effect of fiber morphology on the radial stress in a concentric cylinder due to $\Delta T = -792°C$: (a) cases 1–3; (b) cases 4–6; (c) cases 7–9.

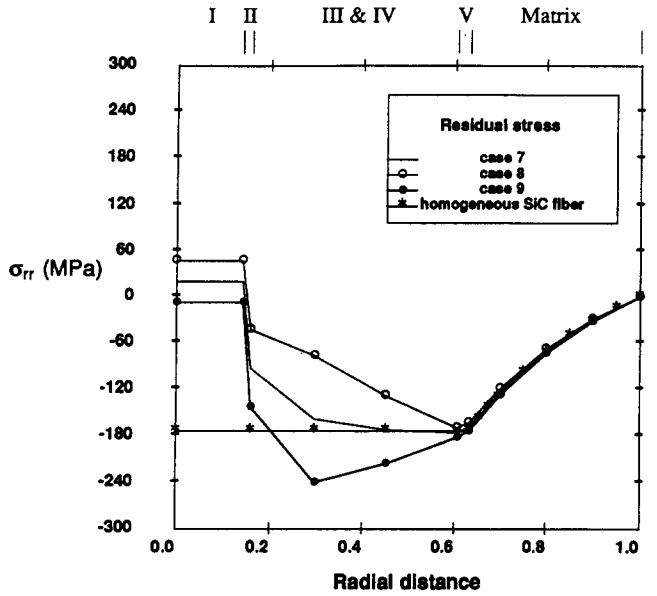

Fig. 5 (*continued*).

sequence reverses the stress distribution in the interfacial region without significantly affecting the stress distribution in the matrix phase. The results presented in the figure clearly indicate a reduction in the matrix hoop stress in the presence of a single interfacial layer with an increasing thermal expansion coefficient for the layer as discussed by Arnold *et al.* (1990). It is seen that beyond a certain value of the thermal expansion coefficient for the interfacial layer, however, a reduction in the matrix hoop stress is accompanied by an increase in the interfacial layer hoop stress as also pointed out by the above authors. The

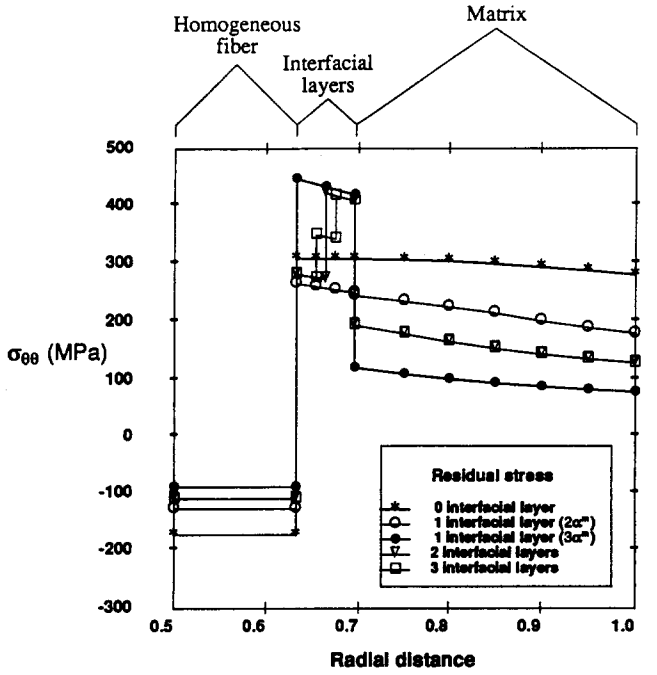

Fig. 6. The effect of interfacial layer morphology on the hoop stress in a concentric cylinder due to $\Delta T = -792°C$.

use of multiple interfacial layers, on the other hand, tends to modulate to a certain extent the stresses in the interfacial region. It appears that a more advantageous hoop stress distribution in the interfacial region can potentially be obtained by grading the thermal expansion properties, albeit at the expense of an increase in the matrix hoop stress. The hoop stress distribution in the matrix phase in the presence of two and three interfacial layers is bounded by the stress distributions for the single interfacial layers. Virtually no difference in the matrix hoop stress distribution is observed when two or three interfacial layers are present. It is interesting to note that the hoop stress distribution in the matrix phase is not significantly different from the one obtained with two or three interfacial layers if a single interfacial layer with the average value of the thermal expansion coefficient is used, i.e. thermal expansion coefficient two and one half times that of the matrix phase. The hoop stress in the interfacial region, in this case, is approximately the average of the hoop stress obtained with the two or three interfacial layers. This suggests that in some situations a single interfacial layer may be sufficient to optimize residual stresses, thus eliminating the additional cost of depositing multiple interfacial layers.

The corresponding results for the axial stress σ_{xx} distributions are illustrated in Fig. 7. For this component of stress, the presence of an interfacial layer results in an increase of the matrix axial stress at the fiber–matrix interface and a decrease in the outer region. Multiple interfacial layers produce potentially more desirable stress distributions in the interfacial region only, and without offering any advantage over the single interfacial layer with regard to the matrix axial stress distribution. As in the preceding case, a single interfacial layer with the average thermal expansion coefficient produces virtually the same axial stress in the matrix phase and an average stress profile in the interfacial region compared to the multiple layers. Similar conclusions can be drawn from the results for the radial stress distributions presented in Fig. 8. Here however, the presence of an interfacial layer results in a decrease in the radial stress distribution throughout the entire region of the concentric composite cylinder. The lowest stress profile is obtained for the single interfacial layer with the highest thermal expansion coefficient. The two and three interfacial layers produce virtually identical stress distributions, which are bounded by the distributions obtained for the single layer cases. Virtually the same distributions are obtained for a single

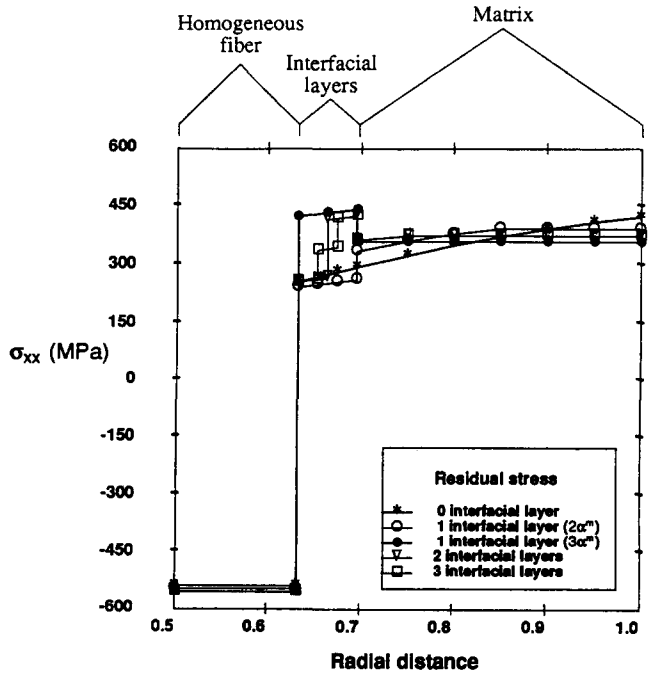

Fig. 7. The effect of interfacial layer morphology on the axial stress in a concentric cylinder due to $\Delta T = -792°C$.

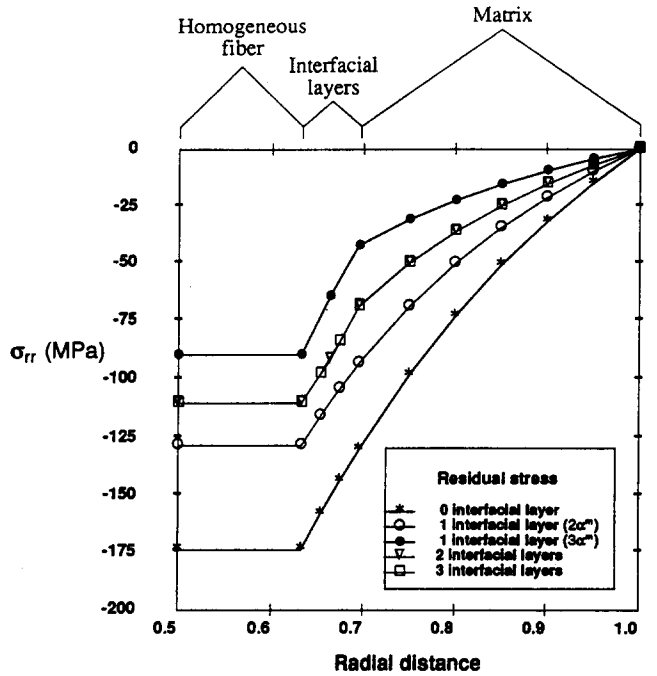

Fig. 8. The effect of interfacial layer morphology on the radial stress in a concentric cylinder due to $\Delta T = -792°C$.

interfacial layer with the average thermal expansion coefficient both in the matrix phase and the interfacial region compared to the multiple layers.

CONCLUSIONS

An efficient method has been outlined for the determination of thermoplastic response of metal matrix composites based on the concentric cylinder geometry. The method is an extension of the local/global stiffness matrix formulation for layered media that has previously been applied to elastic problems. Closed-form expressions have been provided for the local stiffness matrices of isotropic, transversely isotropic and orthotropic layers, in the presence of thermal and inelastic effects. These expressions can be quickly programmed and a simple algorithm for assembling the global stiffness matrix can be constructed for any arbitrarily layered concentric cylinder assemblage. This eliminates the need to resolve the basic problem of a layered concentric cylinder assemblage for the particular geometry under consideration.

The versatility of the method has been illustrated by investigating the effects of fiber and interfacial layer morphologies on the thermally-induced, residual stresses in SiC–Ti_3Al composites. The results indicate that the layered microstructure of the SiC fiber has little effect on the residual stress distributions in the matrix phase of a SiC–Ti composite for the considered fiber volume fraction and material parameters. The stress profiles in the individual layers of the SiC fiber however, are substantially different than the corresponding profiles in a homogeneous SiC fiber embedded in the same matrix material. The layered microstructure of the SiC fiber does not produce substantially different effective properties of the "composite" fiber under axisymmetric thermomechanical loading from those of a homogeneous SiC fiber. The matrix, therefore, sees very little difference in the constraint provided by the homogeneous and layered SiC fiber during thermal loading. Consequently, the stresses at the fiber–matrix interface are not substantially different. On the other hand, the resulting stress profiles in the individual layers of the SiC fiber do depend to a large extent on the degree of orthotropy of the layers' thermal expansion coefficients and elastic moduli. For example, the choice of material properties for the outer carbon coating can significantly affect the hoop (and longitudinal) stresses in that region, either accelerating

or delaying radial microcracking. Relatively large longitudinal, tensile stresses also may be present in the carbon core after cool-down, potentially leading to fracturing of the carbon core at moderate axial deformations. Large tensile, radial stresses at the carbon core interface observed for certain combinations of material properties of the SiC fiber regions point to a potential debonding of the carbon core and/or the pyrolytic coating from the remaining fiber annulus during cool-down or upon tensile loading. Further, a variation in the thermal expansion coefficient in the SiC layers of the order of 25% is sufficient to produce a substantially different stress distribution in these layers for certain combinations of material properties. As a result, accurate knowledge of the properties of the different regions in the SCS6 SiC fiber is indispensible for both the modeling and material development efforts.

With regard to the use of multiple interfacial layers, the results indicate that, for the considered material system, grading the thermal expansion properties of the sublayers in the fiber–matrix interfacial region, while keeping all the other properties constant, produces no reduction of the inplane residual stress distribution in the matrix phase, as compared to the inplane stresses induced by a single interfacial layer with the higher thermal expansion coefficient. In fact, introducing additional interfacial layers with a *smaller* thermal expansion coefficient than the thermal expansion coefficient of a single interfacial layer actually *increases* the inplane residual stresses in the matrix phase over those generated in the presence of the single interfacial layer. Similarly, the axial residual stresses at or near the fiber–matrix interface are not relieved by the interfacial layers. The use of multiple interfacial layers, however, has a potentially beneficial effect on the stress distribution in the interfacial region itself.

Further, the work of Arnold *et al.* indicates that the influence of elastic and inelastic properties of the interfacial region is most dominant when attempting to reduce the stress distribution in that interfacial region without significantly affecting the matrix stresses. This suggests that the use of multiple interfacial layers may offer some advantages over single interfacial layers if both the thermal expansion properties, together with the elastic and inelastic properties, are graded. Grading in this case has the potential to reduce the generally high stresses in the interfacial region when compensating layers are used, thus preventing premature failure. This issue will be addressed in future investigations.

Acknowledgements—The first author thanks the Fatigue and Fracture Branch at the NASA-Lewis Research Center for the NASA-ASEE Summer Faculty Fellowship during the summers of 1991 and 1992 in the course of which this investigation was conducted. Dr DiCarlo provided valuable and timely information on the most up-to-date properties of SCS6 SiC fibers and Dr Lerch supplied the photomicrograph of the cross-section of a SCS6 SiC fiber shown in Fig. 1. The finite-element results presented in Table 2 have been generated by Mr Robert S. Salzar of the Civil Engineering and Applied Mechanics Department at the University of Virginia.

REFERENCES

ABAQUS v4.8 (1989). Hibbitt, Karlsson & Sorensen, Inc., Pawtucket, RI.

Aboudi, J. (1985). The effective thermomechanical behavior of inelastic fiber-reinforced materials. *Int. J. Engng Sci.* **23,** 773–787.

Aboudi, J. (1991). *Mechanics of Composite Materials—A Unified Micromechanics Approach.* Elsevier, The Netherlands.

Arnold, S. M., Arya, V. K. and Melis, M. E. (1990). Elastic/plastic analyses of advanced composites investigating the use of the compliant layer concept in reducing residual stresses resulting from processing. NASA Technical Memorandum 103204, Lewis Research Center.

Arnold, S. M. and Wilt, T. E. (1992). Influence of engineered interfaces on residual stresses and mechanical response in metal matrix composites. NASA Technical Memorandum 105438, Lewis Research Center.

Avery, W. B. and Herakovich, C. T. (1986). Effect of fiber anisotropy on the thermal stresses in fibrous composites. *J. Appl. Mech.* **53,** 751–756.

Brindley, P. K., Draper, S. L., Eldridge, J. I., Nathal, M. V. and Arnold, S. M. (1992). The effect of temperature on the deformation and fracture of SiC/Ti-24Al-11Nb. *Met Trans. A* **23A,** 2527–2540.

Brindley, P. K., MacKay, R. A. and Bartolotta, P. A. (1990). Thermal and mechanical fatigue of a SiC/Ti-24Al-11Nb composite. NASA Technical Memorandum 103279, Lewis Research Center.

Bufler, H. (1971). Theory of elasticity of a multilayered media. *J. Elasticity* **1,** 125–143.

Derstine, M. S. and Pindera, M.-J. (1989). Nonlinear response of composite tubes under combined thermo-mechanical loading. In *Composites and Other New Materials for PVP: Design and Analysis Considerations,* ASME PVP-Vol. 174 (Edited by D. Hui, T. J. Kozik, G. E. O. Widera and M. Shiratori), pp. 19–28. ASME, New York.

DiCarlo, J. A. (1988). High temperature properties of CVD silicon carbide fibers. In *Proc. International Conference on Whisker- and Fiber-Toughened Ceramics* (Edited by R. A. Bradley, D. E. Clark, D. S. Larsen and J. O. Stiegler), pp. 1–8. ASM International, Metals Park, OH.

DiCarlo, J. (1992). Private communication.

Dvorak, J. G. (1990). *Inelastic Deformation of Composite Materials*. Springer, New York.

Fujita, T., Pindera, M.-J. and Herakovich, C. T. (1990). Temperature-dependent tensile and shear response of P100/6061 graphite-aluminium. In *Thermal and Mechanical Behavior of Metal Matrix and Ceramic Matrix Composites*, ASTM STP 1080 (Edited by J. M. Kennedy, H. H. Moeller and W. S. Johnson), pp. 165–182. American Society for Testing and Materials, Philadelphia, PA.

Johnson, W. S., Lubowinski, S. J. and Highsmith, A. L. (1990). Mechanical characterization of unnotched SCS6/Ti-15-3 metal matrix composites at room temperature. In *ASTM STP 1080* (Edited by J. M. Kennedy, H. H. Moeller and W. S. Johnson), pp. 193–218. American Society for Testing and Materials, Philadelphia, PA.

Lara-Curzio, E. and Sternstein, S. S. (1992a). Thermoelastic analysis of composite CVD SiC fibers. *J. Compos. Sci. Technol.* (in press).

Lara-Curzio, E. and Sternstein, S. S. (1992b). The anomalous thermal expansion behavior of chemically vapor deposited silicon carbide fibers. *J. Am. Ceram. Soc.* (in press).

Lekhnitskii, S. G. (1981). *Theory of Elasticity of An Anisotropic Body*. Mir, Moscow.

Lerch, B. A., Hull, D. R. and Leonhardt, T. A. (1988). As-received microstructure of a SiC/Ti-15-3 composite. NASA Technical Memorandum 100938, Lewis Research Center.

Li, Z. and Bradt, R. C. (1986). Thermal expansion of the cubic (3C) polytype of SiC. *J. Mater. Sci.* **26**, 4366–4368.

Lissenden, C. J., Pindera, M.-J. and Herakovich, C. T. (1992a). Stiffness degradation of SiC/Ti tubes subjected to biaxial loading. *J. Compos. Sci Technol.* (in press).

Lissenden, C. J., Pindera, M.-J. and Herakovich, C. T. (1992b). Response of SiC/Ti tubes under biaxial loading in the presence of damage. In *Damage Mechanics in Composites*, ASME AMD-Vol. 150, AD-Vol. 32 (Edited by D. H. Allen and D. C. Lagoudas), pp. 73–90. ASME, New York.

MacKay, R. A., Brindley, P. K. and Froes, F. H. (1991). Continuous fiber-reinforced titanium aluminide composites. *J. Minerals, Metals Mater. Soc.* (May), 23–29.

McKee, J. A. and Joo, L. A. (1972). New carbon monofilament substrate for chemical vapor deposition. In *Proc. 3rd International Conference on CVD* (Edited by F. A. Glaski), pp. 536–551. ANS, Hinsdale, IL.

Mendelson, A. (1983). *Plasticity: Theory and Applications*. Robert E. Krieger, Malabar, FL.

Ning, X. J. and Pirouz, P. (1991). The microstructure of SCS-6 SiC fiber. *J. Mater. Res.* **10** (Oct), 2234–2248.

Pindera, M.-J. (1991). Local/global stiffness matrix formulation for composite materials and structures. *Compos. Engng* **1** (2), 69–83.

Pindera, M.-J. and Freed, A. D. (1992a). Local/global stiffness matrix formulation for axisymmetric elastoplastic problems in composite mechanics. NASA Technical Memorandum (in preparation).

Pindera, M.-J. and Freed, A. D. (1992b). The effect of fiber microstructure on the evolution of residual stresses in titanium matrix composites. In *Topics in Composite Materials and Structures, ASME AD-Vol. 26, AMD-Vol. 133* (Edited by V. Birman and A. Nagar), pp. 21–26. ASME, New York.

Sutcu, M. (1992). A recursive concentric cylinder model for composites containing coated fibers. *Int. J. Solids Structures* **29**, 197–213.

Warwick, C. W. and Clyne, T. W. (1991). Development of composite coaxial cylinder stress analysis model and its application to SiC monofilament systems. *J. Mater. Sci.* **26**, 3817–3827.

Wawner, F. E. (1988). Boron and silicon carbide/carbon fibers. In *Fibre Reinforcements for Composite Materials* (Edited by A. R. Bunsell), pp. 371–424. Elsevier, Amsterdam, The Netherlands.

APPENDIX

The local stiffness matrix elements of transversely isotropic and orthotropic, elastic cylindrical shells, as well as isotropic, inelastic cylindrical shells for axisymmetric, generalized plane strain problems in polar coordinates are given below. For transversely isotropic, elastic and isotropic, inelastic shells with the r–θ plane of isotropy we have:

Elastic contributions

$$k_{11} = \frac{[(C_{0r}+C_{rr})r_{k-1}-(C_{0r}-C_{rr})r_k^2/r_{k-1}]}{r_k^2-r_{k-1}^2},$$

$$k_{12} = \frac{-2C_{rr}r_k}{r_k^2-r_{k-1}^2},$$

$$k_{21} = \frac{-2C_{rr}r_{k-1}}{r_k^2-r_{k-1}^2},$$

$$k_{22} = \frac{[(C_{0r}+C_{rr})r_k-(C_{0r}-C_{rr})r_{k-1}^2/r_k]}{r_k^2-r_{k-1}^2},$$

$$k_{13} = -C_{x\theta},$$

$$k_{23} = C_{x\theta},$$

$$f_1 = [C_{x\theta}\alpha_{xx} + (C_{\theta r} + C_{rr})\alpha_{rr}],$$

$$f_2 = -[C_{x\theta}\alpha_{xx} + (C_{\theta r} + C_{rr})\alpha_{rr}],$$

$$\phi_{11} = -2\pi C_{x\theta} r_{k-1},$$

$$\phi_{22} = 2\pi C_{x\theta} r_k,$$

$$\psi = \pi C_{xx}(r_k^2 - r_{k-1}^2),$$

$$\Omega = -\pi(C_{xx}\alpha_{xx} + 2C_{x\theta}\alpha_{rr})(r_k^2 - r_{k-1}^2).$$

Inelastic contributions

$$g_1 = \frac{2C_{\theta\theta} r_k G_k^+}{r_k^2 - r_{k-1}^2} - \bar{G}_k^-,$$

$$g_2 = -\frac{[(C_{\theta r} + C_{rr})r_k - (C_{\theta r} - C_{rr})r_{k-1}^2/r_k]G_k^+}{r_k^2 - r_{k-1}^2} + \bar{G}_k^+,$$

where

$$G(r) = \frac{1}{2r}\int_{r_{k-1}}^{r} \sum_{i=x,\theta,r} \frac{(C_{ri} + C_{\theta i})}{C_{rr}} \varepsilon_{ii}^{in} r'\, dr' + \frac{r}{2}\int_{r_{k-1}}^{r} \sum_{i=x,\theta,r} \frac{(C_{ri} - C_{\theta i})}{C_{rr}} \varepsilon_{ii}^{in} \frac{dr'}{r'} + \frac{1}{2}\sum_{i=x,\theta,r} \frac{C_{ri}}{C_{rr}} \varepsilon_{ii}^{in}(r_{k-1}) r \left(\frac{r_{k-1}^2}{r^2} - 1\right),$$

$$\bar{G}(r) = \frac{(C_{\theta r} - C_{\theta\theta})}{2r^2}\int_{r_{k-1}}^{r} \sum_{i=x,\theta,r} \frac{(C_{ri} + C_{\theta i})}{C_{rr}} \varepsilon_{ii}^{in} r'\, dr' + \frac{(C_{\theta r} + C_{\theta\theta})}{2}\int_{r_{k-1}}^{r} \sum_{i=x,\theta,r} \frac{(C_{ri} - C_{\theta i})}{C_{rr}} \varepsilon_{ii}^{in} \frac{dr'}{r'}$$
$$+ \frac{1}{2}\sum_{i=x,\theta,r} \frac{C_{ri}}{C_{rr}} \varepsilon_{ii}^{in}(r_{k-1}) \left[C_{\theta r}\left(\frac{r_{k-1}^2}{r^2} - 1\right) - C_{rr}\left(\frac{r_{k-1}^2}{r^2} + 1\right)\right],$$

$$\Pi = 2\pi \int_{r_{k-1}}^{r_k} \sum_{i=x,\theta,r} C_{xi} \varepsilon_{ii}^{in} r'\, dr'.$$

For orthotropic, elastic shells we have

$$k_{11} = \frac{[(C_{\theta r} + \lambda C_{rr}) r_{k-1}^{2\lambda - 1} - (C_{\theta r} - \lambda C_{rr}) r_k^{2\lambda}/r_{k-1}]}{r_k^{2\lambda} - r_{k-1}^{2\lambda}},$$

$$k_{12} = \frac{-2\lambda C_{rr} r_{k-1}^{\lambda - 1} r_k^{\lambda}}{r_k^{2\lambda} - r_{k-1}^{2\lambda}},$$

$$k_{21} = \frac{-2\lambda C_{rr} r_{k-1}^{\lambda} r_k^{\lambda - 1}}{r_k^{2\lambda} - r_{k-1}^{2\lambda}},$$

$$k_{22} = \frac{[(C_{\theta r} + \lambda C_{rr}) r_k^{2\lambda - 1} - (C_{\theta r} - \lambda C_{rr}) r_{k-1}^{2\lambda}/r_k]}{r_k^{2\lambda} - r_{k-1}^{2\lambda}},$$

$$k_{13} = -\left[C_{xr} + (C_{\theta r} + C_{rr})H_1 + \frac{(C_{\theta r} + \lambda C_{rr})(r_{k-1}^{2\lambda} - r_{k-1}^{\lambda - 1} r_k^{\lambda + 1})H_1}{r_k^{2\lambda} - r_{k-1}^{2\lambda}} + \frac{(C_{\theta r} - \lambda C_{rr})(r_{k-1}^{\lambda - 1} r_k^{\lambda + 1} - r_k^{2\lambda})H_1}{r_k^{2\lambda} - r_{k-1}^{2\lambda}}\right],$$

$$k_{23} = \left[C_{xr} + (C_{\theta r} + C_{rr})H_1 + \frac{(C_{\theta r} + \lambda C_{rr})(r_{k-1}^{\lambda + 1} r_k^{\lambda - 1} - r_k^{2\lambda})H_1}{r_k^{2\lambda} - r_{k-1}^{2\lambda}} + \frac{(C_{\theta r} - \lambda C_{rr})(r_{k-1}^{2\lambda} - r_{k-1}^{\lambda + 1} r_k^{\lambda - 1})H_1}{r_k^{2\lambda} - r_{k-1}^{2\lambda}}\right],$$

$$f_1 = \left[C_{xr}\alpha_{xx} + C_{r\theta}\alpha_{\theta\theta} + C_{rr}\alpha_{rr} - (C_{\theta r} + C_{rr})H_2 \right.$$
$$\left. - \frac{(C_{\theta r} + \lambda C_{rr})(r_{k-1}^{2\lambda} - r_{k-1}^{\lambda - 1} r_k^{\lambda + 1})H_2}{r_k^{2\lambda} - r_{k-1}^{2\lambda}} - \frac{(C_{\theta r} - \lambda C_{rr})(r_{k-1}^{\lambda - 1} r_k^{\lambda + 1} - r_k^{2\lambda})H_2}{r_k^{2\lambda} - r_{k-1}^{2\lambda}}\right],$$

$$f_2 = -\left[C_{xr}\alpha_{xx} + C_{r\theta}\alpha_{\theta\theta} + C_{rr}\alpha_{rr} - (C_{\theta r} + C_{rr})H_2 \right.$$
$$\left. - \frac{(C_{\theta r} + \lambda C_{rr})(r_{k-1}^{\lambda + 1} r_k^{\lambda - 1} - r_k^{2\lambda})H_2}{r_k^{2\lambda} - r_{k-1}^{2\lambda}} - \frac{(C_{\theta r} - \lambda C_{rr})(r_{k-1}^{2\lambda} - r_{k-1}^{\lambda + 1} r_k^{\lambda - 1})H_2}{r_k^{2\lambda} - r_{k-1}^{2\lambda}}\right],$$

$$\phi_{11} = \frac{2\pi}{r_k^{2\lambda} - r_{k-1}^{2\lambda}}\left[(C_{x\theta} - \lambda C_{xr}) r_k^{2\lambda} r_{k-1}^{\lambda} \frac{(r_k^{1-\lambda} - r_{k-1}^{1-\lambda})}{1-\lambda} - (C_{x\theta} + \lambda C_{xr}) r_{k-1}^{\lambda} \frac{(r_k^{1+\lambda} - r_{k-1}^{1+\lambda})}{1+\lambda}\right],$$

$$\phi_{22} = \frac{2\pi}{r_k^{2\lambda} - r_{k-1}^{2\lambda}}\left[(C_{x\theta} + \lambda C_{xr}) r_k^{\lambda} \frac{(r_k^{\lambda+1} - r_{k-1}^{\lambda+1})}{1+\lambda} - (C_{x\theta} - \lambda C_{xr}) r_{k-1}^{2\lambda} r_k^{\lambda} \frac{(r_k^{1-\lambda} - r_{k-1}^{1-\lambda})}{1-\lambda}\right],$$

$$\psi = \frac{2\pi H_1}{r_k^{2\lambda} - r_{k-1}^{2\lambda}}\left[(C_{x\theta} + \lambda C_{xr})(r_{k-1}^{\lambda+1} - r_k^{\lambda+1}) \frac{(r_k^{\lambda+1} - r_{k-1}^{\lambda+1})}{1+\lambda} + (C_{x0} - \lambda C_{xr}) \frac{(r_k r_{k-1}^{\lambda} - r_{k-1} r_k^{\lambda})^2}{1-\lambda}\right] + \pi[C_{xx} + (C_{x0} + C_{xr}) H_1](r_k^2 - r_{k-1}^2),$$

$$\Omega = \frac{2\pi H_2}{r_k^{2\lambda} - r_{k-1}^{2\lambda}}\left[(C_{x\theta} + \lambda C_{xr})(r_{k-1}^{\lambda+1} - r_k^{\lambda+1}) \frac{(r_k^{\lambda+1} - r_{k-1}^{\lambda+1})}{1+\lambda} + (C_{x\theta} - \lambda C_{xr}) \frac{(r_k r_{k-1}^{\lambda} - r_{k-1} r_k^{\lambda})^2}{1-\lambda}\right] + \pi\left[(C_{x\theta} + C_{xr}) H_2 - \sum_{i=x,\theta,r} C_{xi}\alpha_{ii}\right](r_k^2 - r_{k-1}^2),$$

where

$$H_1 = \frac{C_{\theta x} - C_{rx}}{C_{rr} - C_{\theta\theta}} \quad \text{and} \quad H_2 = \sum_{i=x,\theta,r}\left(\frac{C_{ri} - C_{\theta i}}{C_{rr} - C_{\theta\theta}}\right)\alpha_{ii}.$$